PNAS NEXUS

PNAS Nexus, 2025, 4, pgaf136

https://doi.org/10.1093/pnasnexus/pgaf136
Advance access publication 28 April 2025
Research Report

The priming phosphorylation of KaiC is activated by the release of its autokinase autoinhibition

Yoshihiko Furuike[a,b], Yasuhiro Onoue[a], Shinji Saito[b,c], Toshifumi Mori[d,e,*] and Shuji Akiyama[a,b,*]

[a]Research Center of Integrative Molecular Systems (CIMoS), Institute for Molecular Science, National Institutes of Natural Sciences, 38 Nishigo-Naka, Myodaiji, Okazaki 444-8585, Japan
[b]Molecular Science Program, Graduate Institute for Advanced Studies, SOKENDAI, 38 Nishigo-Naka, Myodaiji, Okazaki 444-8585, Japan
[c]Department of Theoretical and Computational Molecular Science, Institute for Molecular Science, National Institutes of Natural Sciences, 38 Nishigo-Naka, Myodaiji, Okazaki 444-8585, Japan
[d]Division of Applied Molecular Chemistry, Institute for Materials Chemistry and Engineering, Kyushu University, 6-1 Kasugakoen, Kasuga, Fukuoka 816-8580, Japan
[e]Interdisciplinary Graduate School of Engineering Sciences, Kyushu University, 6-1 Kasugakoen, Kasuga, Fukuoka 816-8580, Japan
*To whom correspondence should be addressed: Email: toshi_mori@cm.kyushu-u.ac.jp (T.M.); Email: akiyamas@ims.ac.jp (S.A.)
Edited By Edward Bayer

Abstract

KaiC, a cyanobacterial circadian clock protein with autokinase activity, catalyzes the dual phosphorylation of its own S431 and T432 residues in a circadian manner in the presence of KaiA and KaiB. Priming phosphorylation at T432 is a key step that promotes secondary phosphorylation at S431. Although KaiA binding is considered essential for KaiC phosphorylation, the mechanisms underlying the activation and inactivation of priming phosphorylation remain elusive. We found that although the priming phosphorylation is autoinhibited within KaiC, it actually proceeds at a rate constant of 0.019 h^{-1} even in the absence of KaiA. The autoinhibition of KaiC and the mechanism underlying the release from autoinhibition by KaiA were examined by KaiC structural analysis and by classical molecular dynamics and quantum mechanics/molecular mechanics simulations. We found that the side chain of T432 adopts two rotamers in dephosphorylated KaiC, one of which places T432 in a position suitable for a nucleophilic attack on the terminal phosphate of adenosine triphosphate. However, the nucleophilicity of T432 was insufficient to overcome an energy barrier of ∼21 kcal mol^{-1} because the catalytic function of a nearby base, E318, was self-suppressed by hydrogen bonding to positively charged R385. Biochemical assays of KaiC mutants showed that the autoinhibition of KaiC autokinase activity is attenuated by conferring T432 high nucleophilicity through the KaiA-assisted release of R385 from E318 to E352. During the circadian cycle, R385 switches interacting partners to inactivate/activate the autokinase function and to ensure the unidirectionality of the KaiC phosphorylation cycle.

Keywords: circadian clock, cyanobacteria, KaiC, kinase, priming phosphorylation

Significance Statement

KaiC, a central player in the circadian clock system of cyanobacteria, undergoes an ordered phosphorylation cycle in the presence of KaiA and KaiB. To elucidate the mechanism underlying the rhythmic regulation of the KaiC autokinase, we performed structural analyses, computational simulations, and biochemical assays of KaiC and its mutants. The results indicate that KaiC is essentially an autoinhibited autokinase, and the autoinhibition of primary phosphorylation at its T432 residue is attenuated by conferring it high nucleophilicity against the terminal phosphate of adenosine triphosphate. KaiA contributes to releasing the autoinhibition of KaiC in a morning phase by switching the interacting partners of R385 from a catalytic glutamate E318 to E352, as well as ensuring unidirectionality of the KaiC phosphorylation cycle.

Introduction

Circadian clocks are time-keeping systems that enable organisms to adapt to daily changes in environmental conditions by modifying intracellular processes. The clock systems from bacteria to mammals share three physiological characteristics (1): self-sustained oscillation with a ∼24-h period, an endogenous period of temperature insensitivity (temperature compensation), and a phase entrainment in response to external stimuli. These properties depend on complex and diverse biochemical events involving clock proteins and clock-related components (2, 3).

Phosphoryl modification is one of the main posttranslational events regulating clock proteins. Phosphorylation of the clock proteins modulates their function, atomic-scale structure, and dynamics, thereby controlling the stoichiometry and stability of multimeric clock–protein complexes (4, 5). Rhythmic phosphorylation of the clock proteins is observed in many organisms

Competing Interest: The authors declare no competing interests.
Received: December 13, 2024. **Accepted:** March 31, 2025

(6, 7) as well as in vitro reconstituted systems (8, 9). To achieve a circadian rhythm of phosphorylation, at least two processes for activating and inhibiting phosphorylation must be present, and these processes must switch appropriately from phase to phase.

Protein kinases phosphorylate targeted amino acids such as Ser, Thr, and Tyr in a substrate molecule or in the kinase itself (autokinase). Kinases can be constitutively active or switch between the active and inactive forms through intermolecular interactions or autophosphorylation (10). The activity of constitutively activate kinases with external substrates can be modulated by the concentration of the substrate. However, the activity of autokinases is controlled by modifying the active site structure or the intramolecular accessibility to the targeted amino acids.

KaiC is a component of the cyanobacterial circadian clock of *Synechococcus elongatus* PCC 7942 that possesses autokinase activity. KaiC is composed of tandemly duplicated N-terminal (CI) and C-terminal (CII) domains (11), and it forms a double-ring hexamer by incorporating one molecule of adenosine triphosphate (ATP) or ADP at every CI–CI and CII–CII interface (12). In the presence of KaiA and KaiB, the S431 and T432 residues in the CII domain of KaiC are phosphorylated/dephosphorylated in a circadian manner (13). The protein undergoes a phosphorylation cycle starting in a fully dephosphorylated form (KaiC-ST) and changing to a T432-phosphorylated form (KaiC-SpT: priming phosphorylation), a S431/T432-phosphorylated form (KaiC-pSpT: secondary phosphorylation), and a S431-phosphorylated form (KaiC-pST) before returning to the KaiC-ST form (14, 15). Studies indicate that the phosphoryl modification of KaiC-ST proceeds only after the addition of KaiA (13). KaiA does not show amino acid sequence or structure similarity with other existing kinases, suggesting that binding of KaiA to KaiC is necessary for the autophosphorylation of KaiC. Although the function and structure of the KaiA–KaiC complex have been studied extensively (16–18), the dynamic nature of the KaiA–KaiC complex has made these studies difficult, and the mechanism underlying the regulation of KaiC autokinase activity remains to be elucidated.

In the absence of KaiA, KaiC is present in the KaiC-ST form under physiological conditions (19–21); therefore, the priming phosphorylation of T432 is frequently discussed in relation to the KaiA binding (13, 18). However, in this study, we found that KaiC is autophosphorylated in the absence of KaiA, albeit at a slower rate. Although this finding is not consistent with the conventional interpretation that KaiC cannot be autophosphorylated in the absence of KaiA, it suggests that the priming phosphorylation of KaiC is activated by releasing the autoinhibition of autophosphorylation activity through interaction with KaiA. This finding provides an opportunity to examine the mechanism by which KaiA activates KaiC autophosphorylation by analyzing the autoinhibition of KaiC without using KaiA.

In this study, we revisited our previous crystal structure of KaiC-ST to examine the mechanism underlying the autoinhibition of KaiC autophosphorylation. The priming phosphorylation of KaiC at T432 was examined using classical molecular dynamics (MD) and quantum mechanics/molecular mechanics (QM/MM) simulations, and the energy barrier for the phosphoryl transfer reaction mediated by the identified catalytic base was estimated. Amino acid substitutions in the catalytic base and regulatory residues nearby suggest a mechanism by which the KaiC autophosphorylation is autoinhibited, and this inhibition is released by interaction with KaiA.

Results

Priming phosphorylation at T432 in KaiC occurs even in the absence of KaiA, albeit at a slower rate

At a standard experimental temperature of 30 °C (19–21), KaiC underwent the autodephosphorylation and was eventually detected in a fully dephosphorylated form, KaiC-ST (Figs. 1A and S1). After 40 h of incubation at 30 °C, a small fraction of KaiC remained in the KaiC-SpT, KaiC-pSpT, and KaiC-pST forms, which did not change detectably after another 20 h.

Next, we performed a densitometric analysis of the gel image (Fig. 1A) and carefully examined the resultant kinetic traces for autodephosphorylation (Fig. 1B). Consistent with previous reports (19–21), the KaiC-SpT and KaiC-pSpT fractions decreased rapidly, whereas the KaiC-pST fraction increased transiently and then began to decrease, and the KaiC-ST form increased progressively. At 40–60 h of incubation, the fractions of KaiC-SpT, KaiC-pSpT, and KaiC-pST remained constant at ~0.03, 0.02, and 0.06, respectively (Fig. 1B, inset). KaiA was previously reported to be essential for the autophosphorylation of KaiC-ST at 30 °C (13). However, the present observations imply that KaiC-ST is autophosphorylated even in the absence of KaiA, albeit at a slower rate.

As shown by solid lines in Fig. 1B, the global fitting of a reversible four-state cyclic model (14, 15) was used to examine the autodephosphorylation dynamics of KaiC, and the eight associated rate constants were determined (Fig. 1C). The contributions of the priming (KaiC-ST → KaiC-SpT, $k_1 = 1.9 \pm 0.3 \times 10^{-2}\ h^{-1}$) and secondary (KaiC-SpT → KaiC-pSpT, $k_2 = 1.7 \pm 0.4 \times 10^{-1}\ h^{-1}$) autophosphorylation events were considerable and reproducible ($n = 5$, Table S1), even when the reaction was initiated using different relative amounts of KaiC in the four states (Fig. S2). When both k_1 and k_2 were forced to zero while keeping the others unchanged, the fitting to the residual phosphorylated species became considerably poorer (Fig. 1B, dashed lines). This result means that the small but nonzero values of k_1 and k_2 make a significant contribution to the autodephosphorylation dynamics in Fig. 1B. Consistent with this interpretation, KaiC, which was dephosphorylated by equilibration at pH 8 for 50 h at 30 °C, was slightly but obviously phosphorylated after the pH was increased to 9.0 (Figs. 1D and S3).

The present data and analysis suggest that the priming phosphorylation of KaiC-ST occurs slowly but continuously in the absence of KaiA, even under steady-state conditions in which KaiC-ST is the predominant form over other phosphorylated forms at 30 °C (Fig. 1B). As illustrated in the model in Fig. 1C, ~60% [$k_{-1}/(k_{-1} + k_2)$] of the minor KaiC-SpT form is directly converted back to KaiC-ST; however, the remaining 40% undergoes secondary autophosphorylation and is restored to the KaiC-ST form by autodephosphorylation in a cyclic manner. At 30 °C, a small amount of KaiC-SpT, the product of the priming phosphorylation, undergoes a repeated cycle of formation and loss even in the absence of KaiA.

One of two rotamers of T432 in KaiC-ST is near ready for the autokinase substrate

The molecular mechanism of the priming phosphorylation remains under debate partly due to the limited spatial resolution of the KaiA–KaiC complex (16–18). The slow but steady priming phosphorylation of KaiC in the absence of KaiA suggests that the structure of KaiC-ST itself could be used to examine this mechanism.

We thus inspected the existing crystal structure of KaiC-ST (22) from the perspective of priming phosphorylation. An ATP molecule bound between two neighboring CII protomers (CII-ATP,

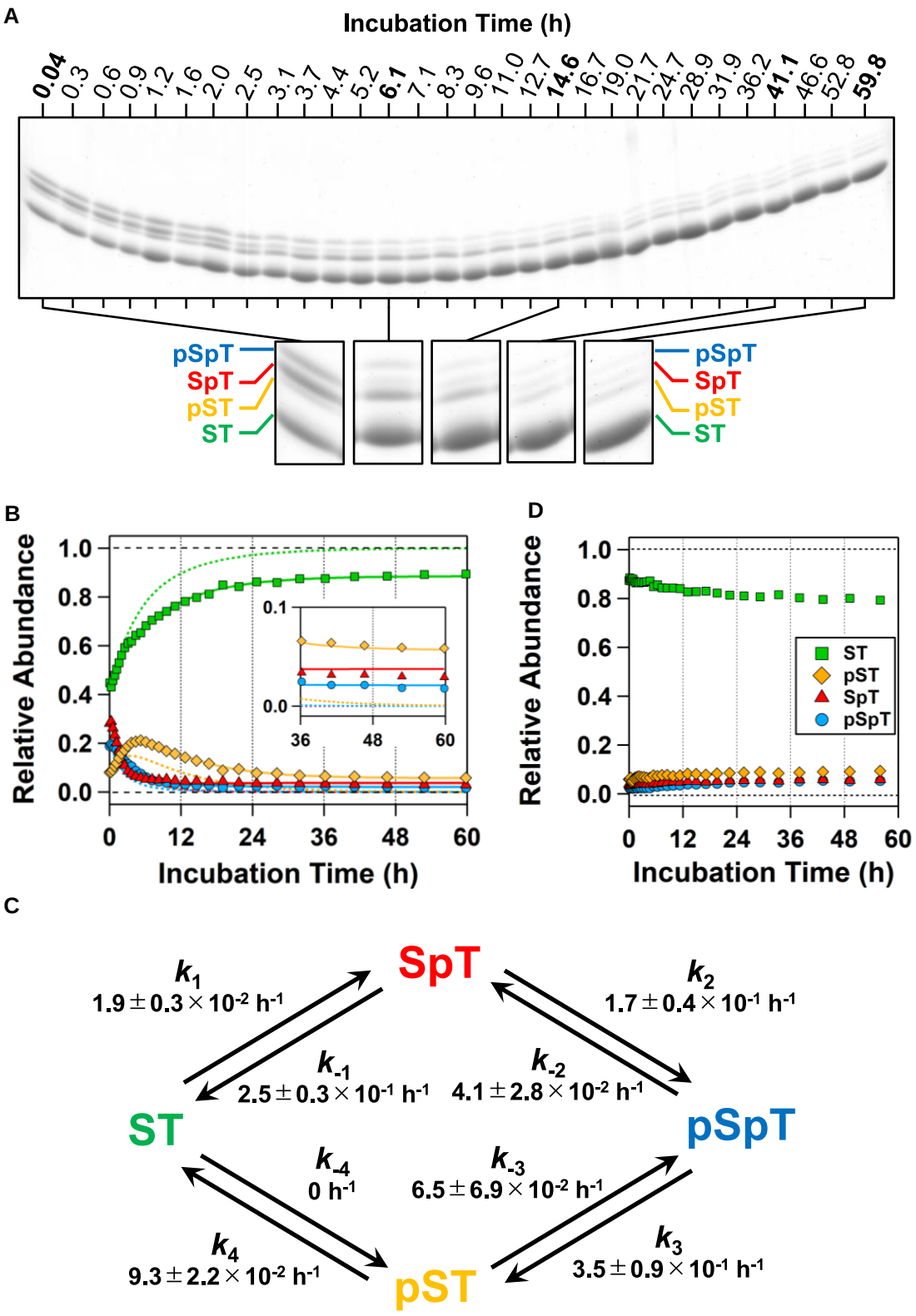

Fig. 1. Priming phosphorylation of T432 in KaiC in the absence of KaiA. A) Representative image of an SDS-PAGE gel loaded with samples from KaiC under autodephosphorylation conditions at 30 °C. To improve the visualization of the four bands corresponding to ST, SpT, pSpT, and pST, the lanes containing the samples collected at 0.04, 6.1, 14.6, 41.1, and 59.8 h are shown in enlarged images. The whole image of the SDS-PAGE gel is available in Fig. S1. B) Densitometric analysis of the gel image in A) was performed to determine the time course of the relative abundance of the ST (squares), SpT (triangles), pSpT (circles), and pST (diamonds) forms. The solid lines represent the best fit from global nonlinear least squares analysis using the four-state model in C). The inset shows the enlarged plots corresponding to the longer period region. Converged rate constants are compiled in Table S1. The dashed lines represent the worse fit obtained by forcing the rate constants for priming (k_1: ST → SpT) and secondary (k_2: SpT → pSpT) phosphorylation to zero and leaving the others unchanged. C) Reversible four-state cyclic model for KaiC phosphorylation/dephosphorylation. Each step (x = 1, 2, 3, and 4) consists of forward (k_X) and backward (k_{-X}) reactions. D) Autophosphorylation of KaiC was induced at 30 °C in the absence of KaiA by increasing the pH from 8.0 to 9.0. The original data for this plot are shown in Fig. S3.

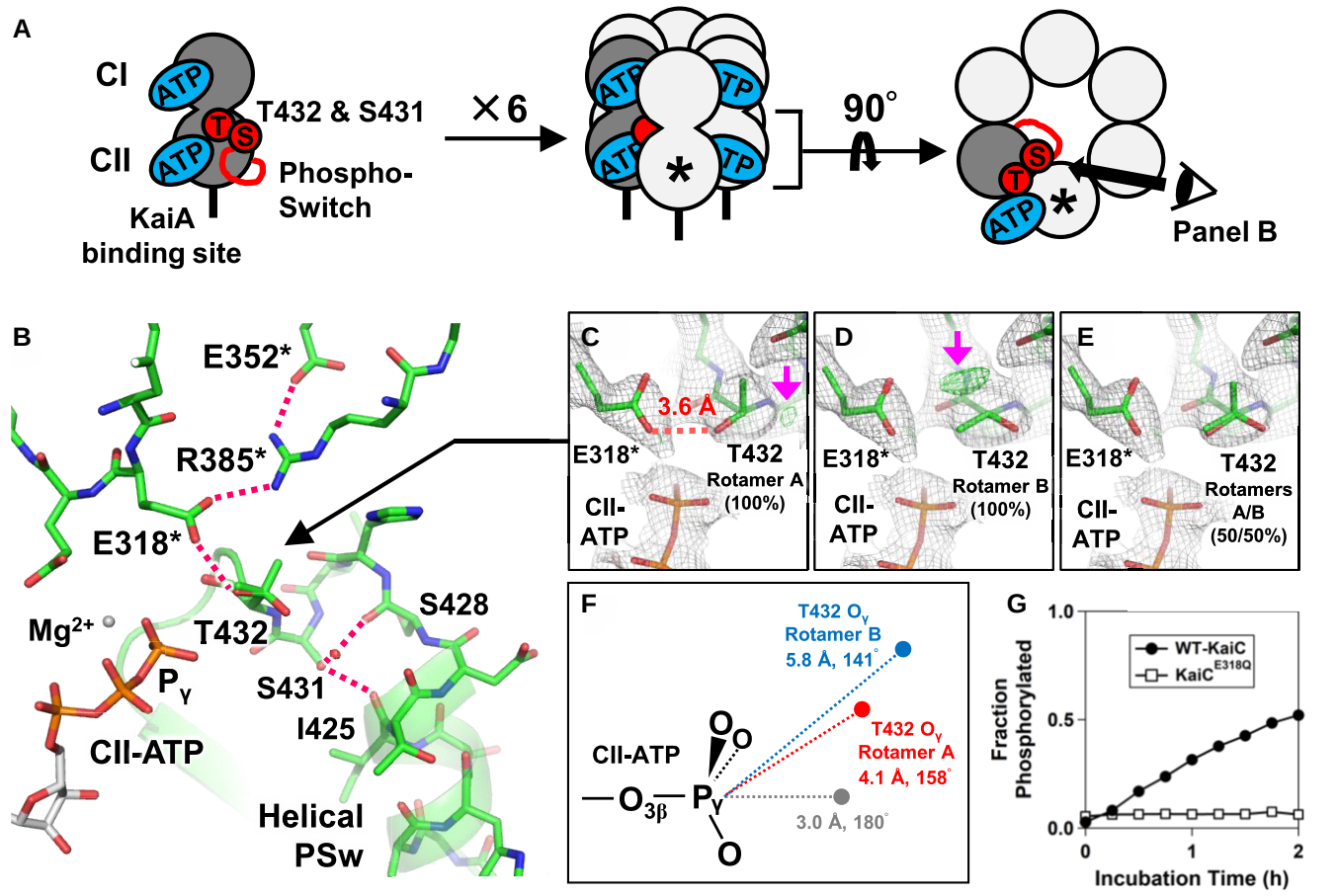

Fig. 2. Structure of KaiC-ST. A) Overall structure of the KaiC-ST hexamer. B) Enlarged image of the autokinase active site around CII-ATP. Hydrogen bonds between the phosphorylation sites (S431 and T432), E318*, R385*, E352*, and PSw are indicated by dashed lines. Residues from a neighboring protomer are indicated by asterisks. C)–E) Occupancy of two rotamers of the T432 side chain. The $2|F_o|-|F_c|$ (gray mesh) and $|F_o|-|F_c|$ difference maps (green mesh) are countered at 1.0- and 3.0-sigma levels, respectively. Magenta arrows indicate the emerged peaks in the $|F_o|-|F_c|$ difference maps. F) Schematic drawing of the positions of T432 O_γ in rotamers A and B. G) Time courses of phosphorylated fraction for wild-type KaiC and KaiC^{E318Q} after KaiA addition (0.04 mg/mL) at time zero.

Fig. 2A) serves as the phosphate source for the kinase reaction. S431, T432, and a phospho-switch (PSw) belonging to one protomer, together with E318*, E352*, and R385* belonging to a second protomer (hereafter, marked with asterisks), constitute an active site around CII-ATP (Fig. 2B). The PSw located at the upstream of S431 undergoes a helix–coil transition according to the phosphoryl modification essentially at S431 (22). In KaiC-ST, the helical conformation of the PSw facilitates positioning of T432 closer to CII-ATP than S431 (Fig. 2B), which is favorable for the priming phosphorylation reaction (22).

The side chain of T432 adopted two conformations corresponding to a rotation of 120° around the C_α–C_β axis. Refinement using only one rotamer (rotamer A), in which the T432 O_γ was oriented toward the phosphorus atom (P_γ) of the γ-phosphate group of CII-ATP, yielded a small but obvious positive difference Fourier peak near T432 C_β (magenta arrow in Fig. 2C). Refinement using the other rotamer (rotamer B) showed a similar but separate peak with the T432 O_γ directed away from CII-ATP (Fig. 2D). The occupancy of each rotamer was estimated at ∼50% (Fig. 2E).

T432 O_γ of rotamer A (T432^{rot-A} O_γ) was nearly configured as a suitable substrate for kinase reactions. In general, Thr or Ser reacts with an ATP molecule through an S_N2-like transition structure (Fig. 2F), in which the nucleophilic O_γ is brought as close as possible to the ATP P_γ along with the ATP P_γ–$O_{3\beta}$ axis to form an O_γ–ATP P_γ bond, and the ATP P_γ–$O_{3\beta}$ bond is then cleaved in a concerted manner. T432^{rot-A} O_γ was only 4.1 Å away from the ATP P_γ with a T432^{rot-A} O_γ–CII-ATP P_γ–CII-ATP $O_{3\beta}$ angle of 158° (Fig. 2F), which is an almost optimal in-line position (∼3 Å and 180°) for the reaction. T432^{rot-B} O_γ was in a less favorable position (5.8 Å and 141°) than T432^{rot-A} O_γ.

To become a ready-to-react nucleophile, the hydroxyl group of T432^{rot-A} has to be deprotonated by a general base. In KaiC-ST, T432^{rot-A} O_γ could potentially be hydrogen-bonded to E318* O_ϵ with a distance of 3.6 Å (Fig. 2C). In fact, the E318Q substitution inhibited the priming phosphorylation in the presence of KaiA (Fig. 2G), suggesting that E318* O_ϵ attracts T432^{rot-A} H_γ through a hydrogen-bonding interaction, and T432^{rot-A} O_γ becomes the reactive nucleophile. These structural analyses suggest that the rotamer A is the structural basis for the slow but steady priming phosphorylation of KaiC-ST.

QM/MM and MD simulations of a proton transfer and T432 phosphorylation reaction

To visualize the priming phosphorylation independent of KaiA, we performed QM/MM metadynamics (metaD) simulation using the KaiC-ST hexamer with T432^{rot-A} as the initial coordinate. In the simulations, we used a QM region consisting of the side chains of T432^{rot-A}, E318*, R385*, and part of CII-ATP/Mg^{2+} (Fig. 3A, represented by green or orange stick models).

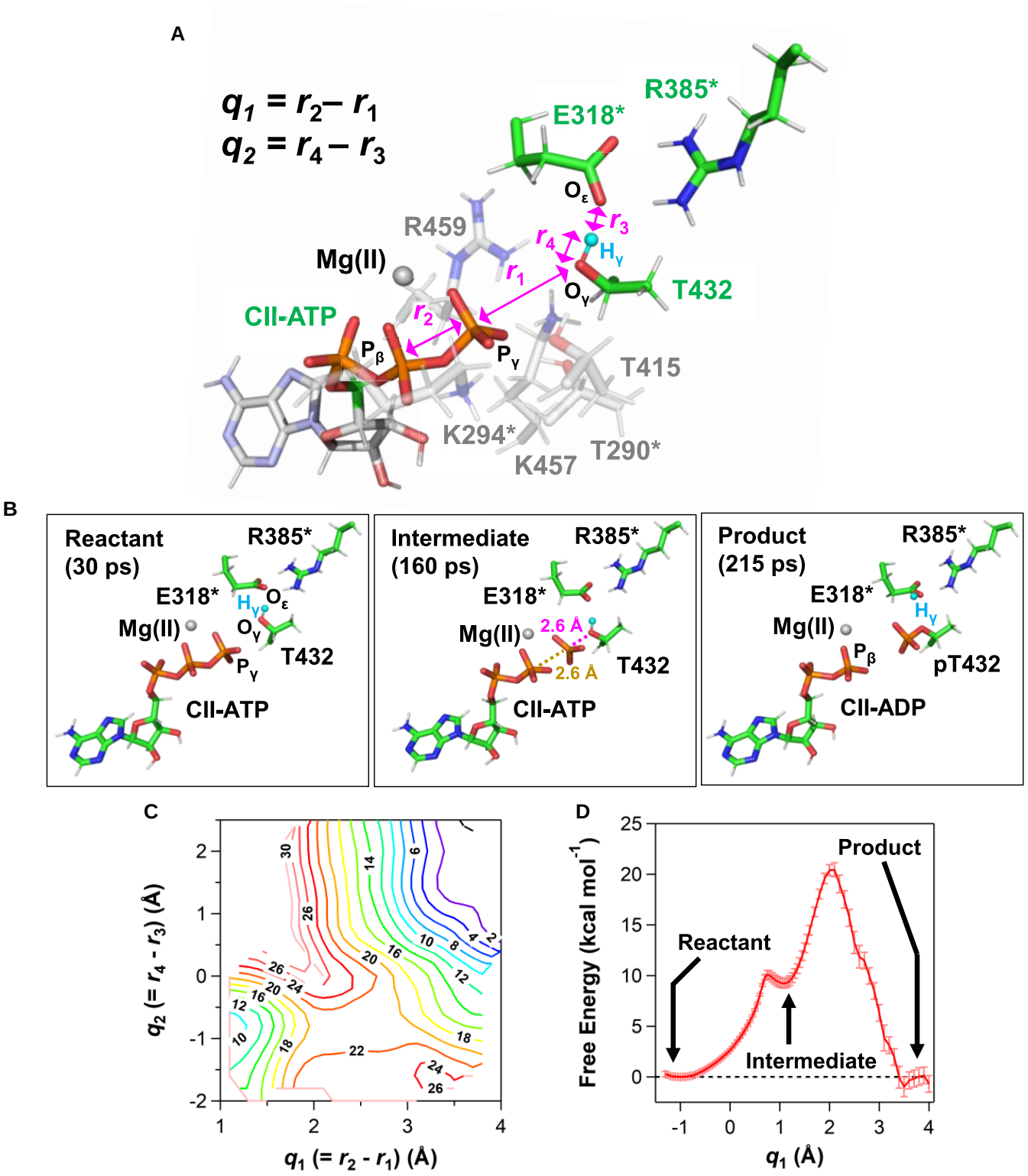

Fig. 3. QM/MM simulations of the phosphoryl transfer from CII-ATP to T432. A) Definition of the QM region and reaction coordinates. The QM region consists of the side chains of T432, E318*, and R385*, triphosphate, and part of the ribose group (C5′, H5′1, and H5′2) of CII-ATP, and Mg^{2+} (green or orange stick models). The hydrogen atom (T432 H_γ) that is transferred from T432 to E318* is highlighted (a cyan sphere). Reaction coordinates are defined as $q_1 = r_2 - r_1$ (r_1: CII-ATP P_γ–T432 O_γ, r_2: CII-ATP P_γ–CII-ATP P_β) and $q_2 = r_4 - r_3$ (r_3: T432 H_γ–E318* O_ε, r_4: T432 H_γ–T432 O_γ). B) Structures obtained during the QM/MM metaD simulation of T432 phosphorylation in KaiC-ST. C) 2D free energy surface calculated using the QM region defined in A). D) Free energy surface along q_1 from the QM/MM calculation. The free energy at the peak top was estimated to be 20.6 ± 0.6 kcal mol^{-1}.

The QM/MM metaD suggested that T432$^{\text{rot-A}}$ O_γ is activated as a nucleophile and attacks CII-ATP P_γ in synergy with E318*. As shown in Fig. 3B, E318* O_ϵ attracted the configured T432$^{\text{rot-A}}$ H_γ through a hydrogen-bonding interaction prior to dissociating the γ-phosphate from CII-ATP, thereby directing the hydroxyl of T432$^{\text{rot-A}}$ to the ready-to-react orientation (reactant in Fig. 3B).

The obtained trajectory shows that the CII-ATP P_γ–CII-ATP $O_{3\beta}$ bond dissociated to form an intermediate state at 160 ps. After remaining in the intermediate state, the system moved to a transition state by decreasing the T432$^{rot\text{-}A}$ O_γ–E318* O_ϵ distance to ∼3 Å; at this moment, a covalent bond was formed between P_γ and T432$^{rot\text{-}A}$ O_γ concomitant with the transfer of T432$^{rot\text{-}A}$ H_γ to E318* (product in Fig. 3B). This suggests that both the formation of the P_γ–T432$^{rot\text{-}A}$ O_γ bond and the proton transfer from T432$^{rot\text{-}A}$ O_γ to E318* O_ϵ must be considered when describing the transition state of the phosphoryl transfer step.

To identify possible reaction pathways, we calculated the 2D free energy surface as a function of the relative positions of CII-ATP P_γ and T432$^{rot\text{-}A}$ H_γ. As the reaction proceeded from the intermediate state (lower left in Fig. 3C), the CII-ATP P_γ–T432$^{rot\text{-}A}$ O_γ distance (r_1) became shorter, whereas the CII-ATP P_γ–CII-ATP P_β distance (r_2) increased ($r_2 - r_1 = q_1$ increased). After the q_1 value reached 2.5, the attraction of T432$^{rot\text{-}A}$ H_γ by E318* O_ϵ shortened the T432$^{rot\text{-}A}$ H_γ–E318* O_ϵ distance (r_3) but lengthened the T432$^{rot\text{-}A}$ H_γ–T432$^{rot\text{-}A}$ O_γ distance (r_4) ($r_4 - r_3 = q_2$ increased). The most plausible reaction pathways emerged as diagonal clefts from the lower left to the upper right corners in Fig. 3C. Together with the 1D free energy surface connecting the reactant and intermediate states (Fig. 3D), the present simulations suggest a barrier as high as ∼21 kcal mol^{-1} to yield KaiC-SpT from KaiC-ST.

In a separate MD simulation, the side chain of T432 in five of the six protomers of KaiC-ST was reoriented to fit the rotamer B during the simulation, whereas one survived as rotamer A for 1 μs mostly within ∼5 Å from CII-ATP P_γ (Fig. S4). This implies that the ready-to-react structures with the short T432$^{rot\text{-}A}$ O_γ–CII-ATP P_γ distance exist in solution in a short-lived state, i.e. a conformationally excited state (23). The high energy barrier and the limited population of ready-to-react structures suggest that the priming phosphorylation of T432 in KaiC-ST is not efficient in the absence of KaiA. This is consistent with experimental observations that only a small amount of pT432 is produced from KaiC-ST at 30 °C (Fig. 1A and B). The accumulation of KaiC-SpT in the presence of KaiA (Fig. 2G) suggests that KaiA plays a role in lowering the energy barrier by enhancing the nucleophilic character of T432$^{rot\text{-}A}$ O_γ.

R385*–E352* hydrogen-bonding pair indirectly regulates the nucleophilicity of T432$^{rot\text{-}a}$ O_γ for priming phosphorylation

The nucleophilicity of T432$^{rot\text{-}A}$ O_γ can be enhanced by strongly withdrawing its proton, T432$^{rot\text{-}A}$ H_γ. The negatively charged carboxylate moiety of E318* appears to be in an ideal position for this purpose. However, its negative charge is partially neutralized by hydrogen bonding with the positively charged guanidino moiety of R385* that is further stabilized by negatively charged E352* (Fig. 2B). We studied the range of the indirect effects on T432$^{rot\text{-}A}$ O_γ by examining the hydrogen-bonding network in KaiC-ST from T432$^{rot\text{-}A}$ O_γ to E318*, R385*, and even E352* (Fig. 2B).

The role of R385* itself was previously discussed based on the observations (24) that the R385A mutant (KaiC^{R385A}) accumulated as mainly phosphorylated states in vivo but as the dephosphorylated state without KaiA in vitro. We revisited the effect of the R385A mutation by analyzing the autodephosphorylation dynamics of KaiC^{R385A} with the global fitting analysis (Fig. 4A). The effect of harboring the guanidino moiety at the 385th position was most obvious in the process of the priming phosphorylation (*t*-test, $P = 1.1 \times 10^{-5}$) (Fig. S5), as the R385A mutation doubled the k_1 value even without KaiA ($k_1 = 3.8 \pm 0.2 \times 10^{-2}$ h^{-1}) (Fig. 4B). This result suggests that R385* neutralizes the negative charge of E318*, eventually suppressing the nucleophilicity of T432^{rot-A} O_γ in KaiC-ST. At the same time, the priming phosphorylation activity of KaiC^{R385A}-ST was further accelerated in the presence of KaiA ($k_1 = \sim 2.0 \times 10^{-1}$ h^{-1}) (Fig. 4C and D), although it was not as high as the activity of KaiA-stimulated KaiC-ST ($k_1 = \sim 3.5 \times 10^{-1}$ h^{-1}) (Fig. 4E). A ratio of the k_1 value in the presence of KaiA to the k_1 value in the absence of KaiA was 18 for KaiC-ST, while it considerably decreased to be ∼5 for KaiC^{R385A}-ST (Fig. 4C). The release of R385* from E318* is necessary to trigger the priming phosphorylation, but not sufficient to increase the nucleophilic reactivity of T432^{rot-A} up to the KaiA-stimulated state of KaiC-ST.

We found that the hydrogen-bond formation R385* and E352* indirectly contributes to the activation by KaiA. A KaiC^{E352Q} mutant in which the charge at the 352nd position was neutralized showed a markedly reduced rate of decrease in the ST state in the presence of KaiA ($k_1 = \sim 1.2 \times 10^{-1}$ h^{-1}) (Fig. 4F) compared with wild-type KaiC (Fig. 4E). Similar observations were made for a KaiC^{E352D} mutant ($k_1 = \sim 1.5 \times 10^{-1}$ h^{-1}) (Fig. 4G) in which the side chain at the 352nd position remained negatively charged, but not sufficiently long enough to form a hydrogen bond with R385*. One possible common reason for the reduced k_1(+KaiA)/k_1(−KaiA) ratios of KaiC^{R385A}, KaiC^{E352Q}, and KaiC^{E352D} (Fig. 4C) is the destabilization of the KaiA-induced state with R385* captured by E352* (Fig. 4H). In the crystal structure of a S431A/T432A mutant (KaiC-AA), which is currently interpreted as the state mimicking KaiC-ST bound by KaiA (25), the side chain of R385* is separated from E318* by a distance of 5.2 Å (Fig. 5B) and trapped by E352* through the hydrogen bonds (Fig. 5A). We speculate that high nucleophilicity T432$^{rot\text{-}A}$ O_γ is continuously achieved by at least two different types of the KaiA-assisted conformational changes of KaiC-ST: locally liberating R385* from E318* and nonlocally forming the hydrogen bonds between R385* and E352*.

R385* rearrangement assures the unidirectionality of the KaiC phosphorylation cycle

The existing library of the KaiC structures (22, 25) suggests the crucial role of R385* rearrangement even after priming phosphorylation. In the T432E mutant (KaiC-SE), which is considered as the best KaiC-SpT mimetic (14, 26), R385* is pulled away from E318* by hydrogen bonds with E432 and E352* (Fig. 5C), leaving E318* activated as the reactive base suitable for attracting a hydrogen atom. This orientation of R385* in KaiC-SE may be effective in promoting the E318*-mediated activation of S431 O_γ for the secondary phosphorylation reaction.

In nine of the 15 pSpT protomers in the library (Fig. 5D, right), the positively charged guanidino moiety of R385* was trapped by the negatively charged side chain of D417*. Although R385* in the other six protomers remained within the interaction range of E352*, the distance between R385* and E318* was considerably longer than the hydrogen-bonding distance (Fig. 5D, left). These findings suggest that E318* of KaiC-pSpT remains as the active free base, despite the lack of reactive side chains for the kinase reaction around CII-ATP. In such an arrangement of R385*, however, KaiC-pST could be autophosphorylated again and reconverted to KaiC-pSpT. In seven of the 10 pST protomers in the library, the side chain of T432 in KaiC-pST, which may restrain this reverse reaction, formed a third rotamer C (Fig. 5E) with its hydroxyl group oriented away from E318* and trapped by R385* (Fig. 5E, left).

The recent cryogenic electron microscopy (cryo-EM) structure of KaiC-pST-mimetic mutant (27), in which the CI and CII domains are stacked close to each other, also shows a similar side chain

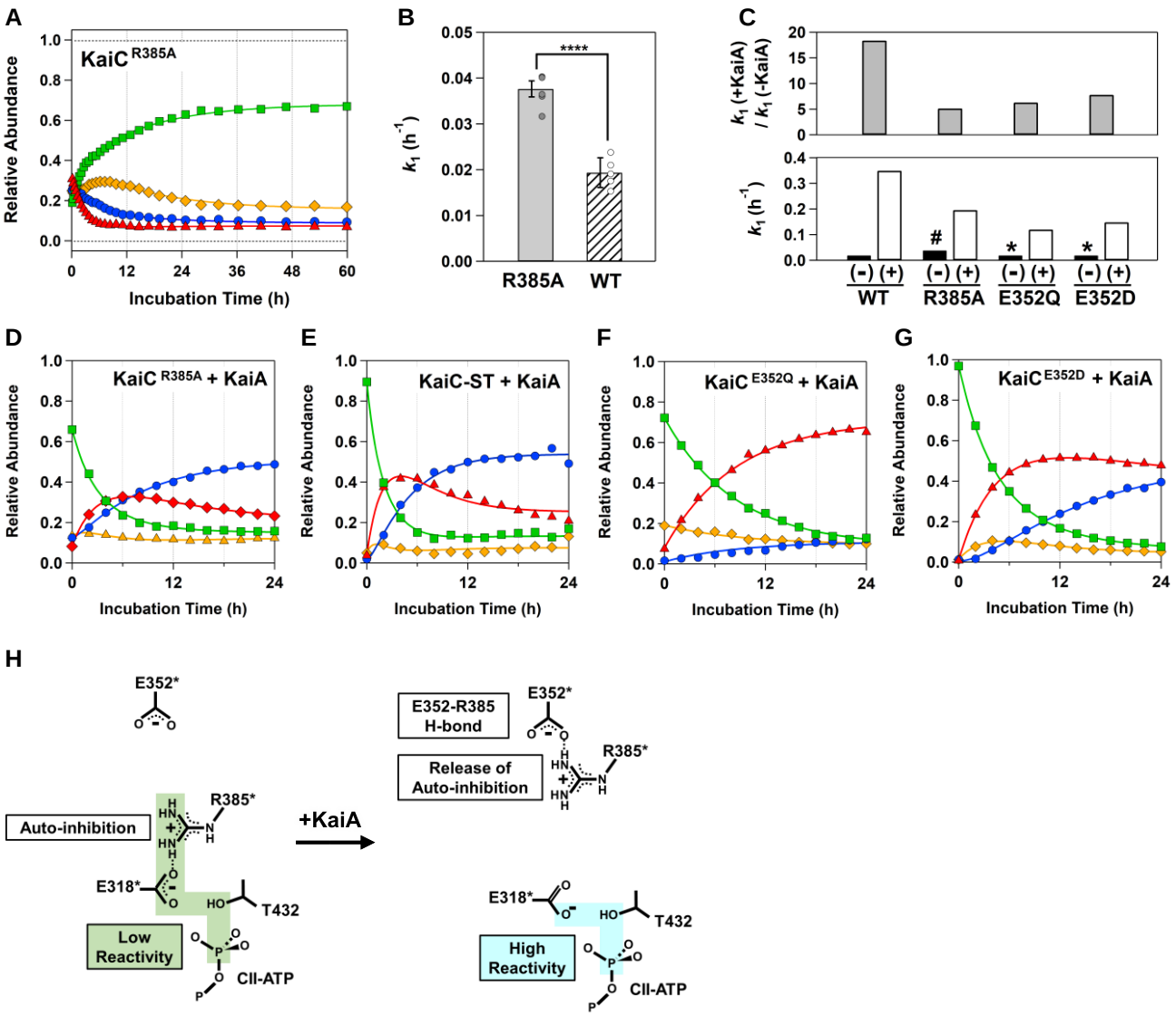

Fig. 4. Local and nonlocal effects on the nucleophilicity of T432$^{rot\text{-}A}$ O_γ. A) Autodephosphorylation dynamics of KaiC^{R385A} (ST: squares, SpT: triangles, pST: diamonds, and pSpT: circles). The solid lines represent the best fit from global nonlinear least squares analysis using the four-state model in Fig. 1C. B) Effect of the R385A substitution on the rate (k_1) of the priming phosphorylation. t test; ****more significant ($P < 0.0005$). See details in Fig. S5. C) Ratios of the k_1 value in the presence of KaiA (+) to the k_1 value in the absence of KaiA (–). #0.038 h^{-1}. *The same k_1 value as wild-type KaiC-ST (0.019 h^{-1}) is assumed for KaiC^{E352Q} and KaiC^{E352D}. D)–G) Time courses of four phosphorylation states of KaiC^{R385A} (+KaiA), KaiC-ST (+KaiA), KaiC^{E352Q} (+KaiA), and KaiC^{E352D} (+KaiA), respectively, at 30 °C. The correspondence of the fitted lines and graph markers is the same as in A). KaiC-ST, KaiC^{E352Q}, KaiC^{E352D}, and KaiC^{R385A} (0.2 mg/mL) were preincubated at 30 °C for 48 h and then at time zero mixed with KaiA at a final concentration of 0.04 mg/mL. H) Schematic drawing of possible hydrogen bonds (black dotted line) and T432$^{rot\text{-}A}$ H_γ-withdrawing reactivity of E318* to enhance the nucleophilicity of T432$^{rot\text{-}A}$ O_γ.

orientation. The side chain of T432 has not been identified in the cryo-EM structure, but its E318*, E352*, R385*, and CII-ATP can be locally superimposed to those in the crystal structure of the unstacked form (Fig. S6A and B), except for the ADP-bound CII–CII interface in the cryo-EM structure (Fig. S6C). Therefore, at least in the KaiC-pST protomer with CII-ATP nearby, rotamer C is considered as the key factor preventing the rephosphorylation of T432.

The coil-to-helix transition of PSw (22), which is promoted by the autodephosphorylation of pS431, returns R385* to the configuration observed in KaiC-ST (Fig. 5A). During the circadian cycle, the positively charged guanidino group of R385* swaps interacting partners among E318*, E352*, and D417* to achieve inactivation/activation of T432$^{rot\text{-}A}$ O_γ, thereby ensuring the unidirectionality of the phosphorylation cycle of KaiC.

Discussion

Although KaiA is considered essential for the phosphorylation of KaiC (13), the present findings clearly demonstrate that the priming phosphorylation of T432 occurs at 30 °C in the absence of KaiA, albeit at a slower rate. Even under conditions that promote the steady-state predominance of KaiC-ST, <10% of KaiC is transiently expressed as partly or fully phosphorylated forms and constantly cycling among the four states (Fig. 1C). The low abundance of these forms is mainly due to inefficient priming phosphorylation, which is limited by the three factors described below.

The first is the marginal stability of the helical PSw in KaiC-ST in solution. The structure of the PSw changed from a helical to a non-helical form in five of six protomers in the QM/MM simulation

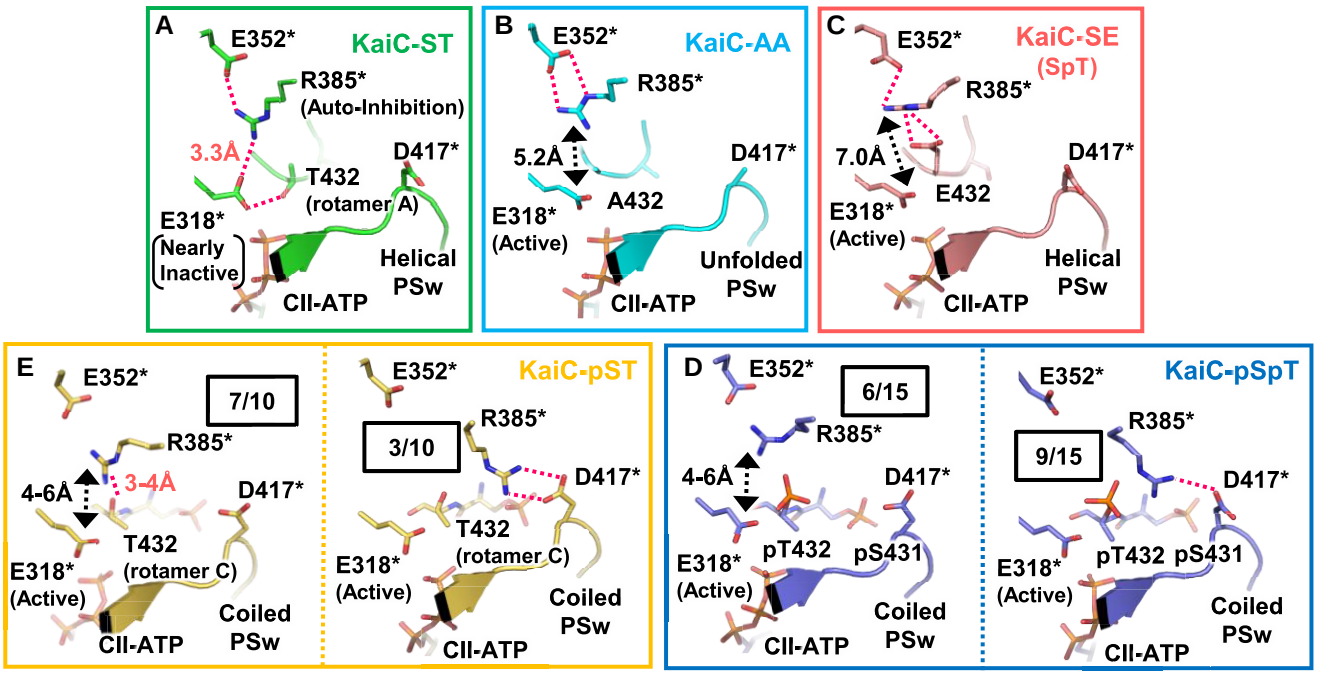

Fig. 5. R385* rearrangement during the circadian cycle. The side chain orientations of R385* in A) KaiC-ST (PDB code: 7DYJ), B) KaiC-AA (PDB code: 7DYE), C) KaiC-SpT (PDB code: 7DYI), D) KaiC-pSpT (PDB code: 7DXQ, 7DY1, and 7V3X), and E) KaiC-pST (PDB code: 7DY1, 7V3X, and 7DY2) are shown. The numbers enclosed in boxes indicate the fractions of the protomers with the corresponding conformation of R385* in the structure library. Hydrogen bonds are indicated by dashed lines. Interatomic distances beyond hydrogen-bonding distance are indicated by dashed arrows.

over a period of 1 μs. This observation is also consistent with our recent mutation study (28), which identified structural polymorphisms of the PSw in KaiC-ST mimetics. The helix-to-coil transition of the PSw causes the hydroxyl group of T432 to face the opposite direction to CII-ATP (Fig. 5E), and the resultant location of T432 downstream of the coiled PSw is unfavorable for the kinase reaction.

The second limiting factor is the rotamers of T432 located downstream of the helical PSw. In KaiC-ST carrying the helical PSw, the side chain of T432 shuttles between the two rotamers A and B, waiting for a chance to attack CII-ATP P_γ. Considering that one half of the rotamers in one-sixth of the KaiC-ST protomers are enabled to react, the fraction of T432 that can undergo the kinase reaction is estimated to be ∼10%.

This ∼10% of the population is limited by the third factor, an energy barrier that can be as high as 21 kcal mol^{-1}. The barrier-crossing mechanism can be largely categorized into base-assisted and substrate-assisted mechanisms (29), which differ in the pathway for withdrawing a proton from the hydroxyl group of Ser or Thr. In the base-assisted mechanism, the substrate proton is transferred to a basic residue nearby, for example, from T432$^{rot\text{-}A}$ O_γ to E318* O_ϵ in KaiC-ST in the absence of KaiA (Fig. 3B). By contrast, in the substrate-assisted mechanism, the substrate proton is directly transferred to one of the three oxygen atoms of the γ-phosphate. The following observations support that the priming phosphorylation occurs in a base-assisted manner. The lone pair of E318* is directly oriented toward T432$^{rot\text{-}A}$ O_γ, whereas CII-ATP O_γ closest to T432 is already involved in a hydrogen bond with T290* and an electrostatic interaction with K294* (Fig. S7). The current QM/MM metaD simulation also found the hydrogen bond between E318* O_ϵ and T432$^{rot\text{-}A}$ H_γ prior to the dissociation of the CII-ATP P_γ–CII-ATP $O_{3\beta}$ bond (Fig. 3B), and the free energy surfaces further support this mechanism (Fig. 3D). Furthermore, the E318Q substitution suppressed the kinase activity in the presence of KaiA (Fig. 2G). These factors led us to conclude that the priming phosphorylation of KaiC-ST follows the base-assisted mechanism, regardless of the presence of KaiA.

It is important to discuss our observations with respect to previous QM/MM studies (see (30) and references are therein). QM/MM simulations have been used to investigate phosphoryl transfer reactions in several kinases, including cAMP-dependent protein kinase (31–35), cyclin-dependent kinase (36–38), and N-acetyl-L-glutamate kinase (39, 40). In these examples, the activation energy for the phosphoryl transfer reaction ranges from 10 to 25 kcal mol^{-1}. The present QM/MM simulation is the first example of the visualization of atomic-scale details before and after the phosphoryl transfer reaction in clock proteins. The reason for this is that high-resolution structures of fully dephosphorylated clock proteins were not available for a long time, as is the case for KaiC (22). The activation energy for T432$^{rot\text{-}A}$ in KaiC-ST, which is ∼21 kcal mol^{-1}, is within the above range, suggesting that once formed, it can be phosphorylated on a reasonable time scale even in the absence of KaiA. According to the Eyring equation, the present experimental rate constant ($k_1 = 1.9 \pm 0.3 \times 10^{-2}$ h^{-1}) for the priming phosphorylation of T432 without KaiA corresponds to an activation energy of 25 kcal mol^{-1}. The discrepancy may be due to the setup or the limited accuracy of our QM/MM calculations, although it may also mean that the contribution of the second factor is larger than the above estimate.

The present results suggest that the binding of KaiA attenuates at least one of the limiting factors for the priming phosphorylation of KaiC-ST. The structural and QM/MM evaluations clearly indicate that the carboxylate side chain of E318* attracts T432$^{rot\text{-}A}$ H_γ and enhances the nucleophilicity of T432$^{rot\text{-}A}$ O_γ (Fig. 3B). This function of E318* as the inherent base is, however, self-suppressed in KaiC-ST by the neutralization of its negative charge with the positively charged guanidino group of R385* nearby. As demonstrated using a series of KaiC mutants (Figs. 4 and 5B), binding of

KaiA attenuates this self-suppression by sequestering R385* from E318* to E352*. The observed decay of the KaiC-ST form in the presence of KaiA (Fig. 4E) suggests that the rate constant of the priming phosphorylation reaction should increase by a factor of 18 (Fig. 4C). This is equivalent to a reduction of the energy barrier of ~2 kcal mol^{-1} caused by enhancing the nucleophilicity of the substrate through the KaiA–KaiC interaction. The present results show that the priming autophosphorylation is self-suppressed, although not completely, in KaiC-ST, whereas that KaiA attenuates this self-suppression to achieve the KaiC autophosphorylation on a reasonable time scale as a circadian clock system.

Since the present study uses the fully dephosphorylated hexamer for analysis, it is worth discussing possible effects of phosphorylated protomers being adjacent to a KaiC-ST protomer. As far as we know, the helical PSw and T432 O_γ in rotamers A and B are observed only in the crystal structure (PDB ID: 7DYJ) of the fully dephosphorylated hexamer analyzed in this study. In a different crystal structure (PDB ID: 7DY2) (22), KaiC is found as the hexamer consisting of one KaiC-ST protomer and five KaiC-pST protomers. This KaiC-ST protomer of 7DY2, which is trapped as a conformation with the coiled PSw and T432 O_γ in rotamer C, would have to overcome an energy barrier >21 kcal mol^{-1} for the priming phosphorylation. In the structure of the KaiC-ST-mimetic mutant (S431C/T432 V), V432 C_γ well mimics T432 O_γ in rotamer B due to the influence of the PSw stabilized as an intermediate conformation between helical and coiled forms (28). Thus, the conversion of rotamers from C to A/B in the transition from the KaiC-pST to KaiC-ST states is not a simple event caused solely by the local interactions around T432 O_γ, but is a complex event driven by the coil-to-helix transition of the PSw structure that is under the further influence of the interprotomer contacts. Since rotamer C is the important factor that prevents T432 in the KaiC-pST protomers from being rephosphorylated (Fig. 5E), it is reasonable to suggest that both the local and nonlocal constraints on T432 O_γ rotamers contribute to drive the KaiC phosphorylation cycle in one direction. We believe this view is essentially consistent with the previous domain-scale explanation (26, 41) that the unidirectionality emerges from the conformation switching between the stacked and unstacked forms of KaiC (Fig. S6).

Common protein kinases are maintained mostly inactive in the absence of activating upstream stimuli, whereas inhibitory factors are removed at the biologically appropriate times and locations. As reviewed in detail by Reinhardt and Leonard (10), there are many systems for maintaining protein kinases inactive, such as blocking ATP binding (42), sequestration of substrates or blocking their access (43–46), occupation or occlusion of catalytic cleft (47–49), and binding of regulatory proteins (50).

In most of these examples, positively charged side chains located within hydrogen-bonding distance to the catalytic glutamate/aspartate are extremely limited. Conserved downstream Lys residues that are intrinsically close to the catalytic aspartate (3.3–4.7 Å) are unlikely to form stable hydrogen bonds, regardless of their activation or inactivation, because the carboxylate plane of the catalytic aspartate is almost perpendicular to the orientation of the Lys (Fig. S8A). This is also the case for casein kinase 1 delta (51), which is essential for the pacemaker function of mammalian clock systems (52). Insulin receptor kinase (42) and the Src family of tyrosine kinases (45) are exceptions because their catalytic aspartate forms a hydrogen bond with the Arg residue located two or four residues downstream; however, these kinases are not in the ATP-bound form (Fig. S8B). This means that, in contrast to KaiC, most protein kinases switch between the active and inactive forms by regulating the substrate access and by autophosphorylating their activation loop (53–56); their catalytic aspartates thus remain unsuppressed to efficiently withdraw a proton from the substrate. KaiC encapsulates both a braking function to fulfill the circadian timescale through the interaction of R385* and E318* and an accelerating function to promote the priming phosphorylation in a morning phase through the interaction of R385* and E352*.

The priming phosphorylation in KaiC can be summarized as follows. The side chain of T432, which was sequestered as the rotamer C in KaiC-pST (Fig. 6A), shuttles between two rotamers, A and B, in KaiC-ST to optimize its attack of CII-ATP P_γ (Fig. 6B). The primary phosphorylation proceeds, albeit slowly, in the ST state even in the absence of KaiA, but its efficiency is low because the function of E318* as the catalytic base to enhance the nucleophilicity of T432 O_γ is autoinhibited by R385* (Fig. 6C). KaiA binds to the C terminus of KaiC (16, 17) and releases this autoinhibition by switching the interacting partner of R385* from E318* to E352* (Fig. 6D). The increased negative charge of E318* facilitates the attraction of $T432^{rot\text{-}A}$ H_γ, resulting in the concerted proton transfer from $T432^{rot\text{-}A}$ to E318* and the nucleophilic attack against CII-ATP P_γ by $T432^{rot\text{-}A}$ O_γ (Fig. 6D). In KaiC-SpT (Fig. 6E), R385* remains evacuated from E318* by the phosphorylated T432 to promote the secondary phosphorylation at S431. Since autodephosphorylation also requires the activation of water molecules or phosphate groups by a general base, we believe that this study will contribute to the elucidation of not only phosphorylation but also less understood autodephosphorylation in KaiC.

Materials and methods

Expression and purification of KaiC and its mutants

Glutathione S-transferase (GST)-tagged KaiC was constructed in the plasmid vector, pGEX-6P-1. GST-tagged KaiC was expressed in *E. coli*. BL21 (DE3) and purified as previously reported (14). The purified KaiC was dissolved in a buffer containing 20 mM Tris–HCl (pH 8), 150 mM NaCl, 1 mM ATP, 5 mM $MgCl_2$, 0.5 mM ethylenediaminetetraacetic acid (EDTA), and 1 mM dithiothreitol (DTT) (buffer A).

KaiC autodephosphorylation assay

WT-KaiC and $KaiC^{R385A}$ (0.6 mg/mL) were incubated at 30 °C to induce autodephosphorylation. Aliquots were taken from the incubated samples at pseudologarithmic intervals using the automated sampling device (57) to cover fast and slow relaxations quantitatively. The relative abundance of four phosphorylated KaiC forms was quantified by sodium dodecyl sulfate polyacrylamide gel electrophoresis (SDS-PAGE) using LOUPE software (57). Kinetic traces for autodephosphorylation dynamics were fitted using a reversible four-state cyclic model as shown in Fig. 1C using MATLAB software.

KaiC autophosphorylation assay

WT-KaiC was preincubated in buffer A for 50 h at 30 °C to induce autodephosphorylation. The pH of the sample solution was changed using a buffer consisting of 20 mM Tris–HCl (pH 9), 150 mM NaCl, 1 mM ATP, 5 mM $MgCl_2$, 0.5 mM EDTA, and 1 mM DTT in a desalting column, PD MiniTrap G-25 (Cytiva). The sample solution at pH 9 (0.4 mg/mL) with abundant KaiC-ST was incubated at 30 °C. Sampling and analyses were performed as described for the autodephosphorylation assay.

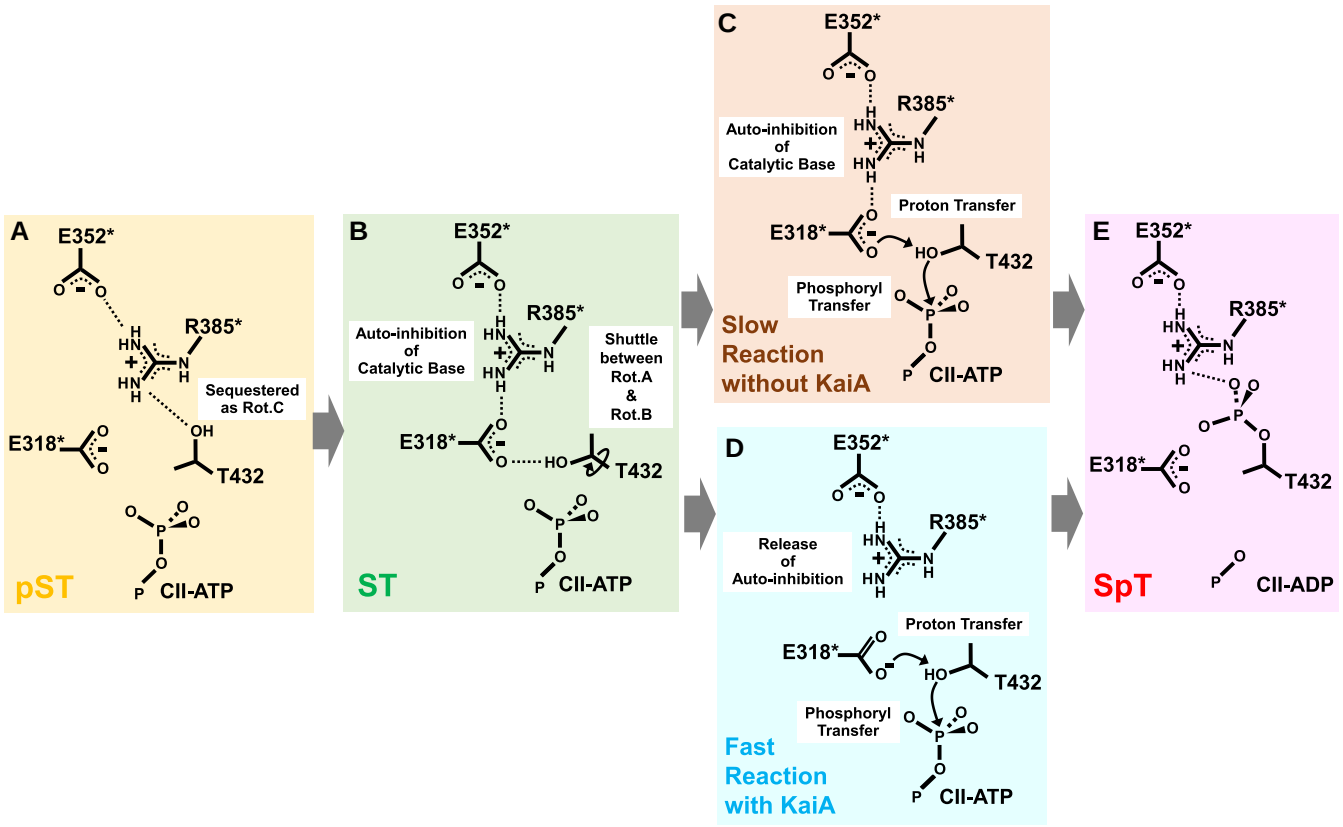

Fig. 6. Proposed reaction scheme for priming phosphorylation at T432 in KaiC. A) KaiC-pST, B) KaiC-ST, C) a reaction intermediate without KaiA, D) the KaiA-assisted state, and E) KaiC-SpT.

KaiA-assisted phosphorylation assay

WT-KaiC and the KaiC mutants KaiC^{R385A}, KaiC^{E352Q}, and KaiC^{E352D} were preincubated in buffer A for 48 h at 30 °C to induce autodephosphorylation. The KaiC solutions (0.2 mg/mL) were then mixed with KaiA (0.04 mg/mL), and the phosphorylation status was analyzed by SDS-PAGE.

Analysis of the crystal structure of KaiC

In this study, the seven coordinates (PDB code: 7DYJ, 7DYE, 7DYI, 7DY1, 7DY2, 7DXQ, and 7V3X) deposited in the Protein Data Bank (PDB) were used for the analysis. The graphical presentations were generated by using Pymol.

QM/MM and MD simulations

The initial coordinates of the KaiC-ST hexamer with T432$^{rot\text{-}A}$ were obtained from PDB: 7DYJ, and the loops that were missing from the crystal structure were modeled according to the previously reported structure (PDB: 2GBL) (17). The flexible N and C termini of KaiC-ST were omitted, i.e. residues I18–I497 of each KaiC-ST monomer were used. In addition, 12 ATP molecules, 12 magnesium ions, and crystal water molecules within the protein molecules were included in the system. Hydrogen atoms were added using the LEAP module in AmberTools. The KaiC-ST hexamer was surrounded by a water layer of 11.0 Å thickness and placed in a rectangular box. Sodium ions were added to neutralize the system charge. The total number of atoms in the system was thus ~207,000.

The Amberff99SB-ILDN force field (58) was used for the protein molecules, with modified parameters for ATP (59). The TIP3P model (60) was used for the water molecules. Long-range electrostatic interactions were treated using the particle mesh Ewald method (61), whereas short-range nonbonded interactions were cut off at 10 Å. A time step of 2 fs was used, and the simulations were performed using the Amber 2018 software (62) and the PLUMED 2.5.3 package (63).

The energy of each system was minimized for 1,000 steps while allowing only hydrogens to relax, followed by energy minimizations of 10,000 steps with restraints on backbone atoms to relax the side chains and 10,000 steps without restraints. The temperature of the system was then gradually increased to 300 K over 100 ps while restraining the backbone atoms with a weak force constant of 1.0 kcal mol^{-1}. Next, a constant-NPT (300 K, 1 atm) simulation was performed for 500 ps under the same restraint, followed by another 500 ps of constant-NPT (300 K, 1 atm) simulation without restraints. Finally, a 10-ns constant-NVT (300 K) simulation was performed to complete the equilibration steps. The temperature was maintained using the Langevin thermostat with a collision frequency of 1.0 ps^{-1}.

The mechanism of the phosphoryl transfer reaction was studied using the structure obtained after the equilibration steps described above. The interface between the protomers B and C, where the T432$^{rot\text{-}A}$ O_γ–CII-ATP P_γ distance was kept short during the 1-μs trajectory, was used. The QM/MM method was used to study the chemical reaction. The QM region consists of the side chains of T432, E318*, and R385*, triphosphate and part of the ribose group (C5′, H5′1, and H5′2) of CII-ATP, and Mg^{2+}. Link atoms are introduced to saturate the valence of the QM boundary atoms. To explore the conformational space efficiently, the density-functional tight-binding method with third-order correction (DFTB3) (64) was chosen as the QM method. The time step was decreased to 0.5 fs in the QM/MM simulations, and the system was

equilibrated using the QM/MM Hamiltonian for 100 ps prior to the following calculations.

To obtain the initial reaction path starting from the reactant state, we performed a metaD simulation (65) using the defined QM region. The difference ($q_1 = r_2 - r_1$) between two distances, r_1: T432$^{rot\text{-}A}$ O_γ–CII-ATP P_γ and r_2: CII-ATP P_γ–CII-ATP P_β, was chosen as the reaction coordinate (Fig. 3A). Although we were interested in the breaking of the CII-ATP P_γ–CII-ATP $O_{3\beta}$ bond, r_2 was used to avoid the effect of permutations between the three CII-ATP O_β atoms. In the metaD simulation, a Gaussian potential of width = 0.20 Å and height = 0.10 kcal mol^{-1} was added every 0.1 ps. Half-harmonic potentials at $q_1 \geq 5.7$ and $q_1 \leq 3.3$ Å with a force constant of 100.0 kcal mol^{-1} Å^2 were applied. The metaD simulation was performed for 300 ps.

To calculate the free energy surface of the reaction, replica exchange umbrella sampling (REUS) simulations were performed (66). The reaction was divided into two parts: the initial CII-ATP P_γ–CII-ATP $O_{3\beta}$ bond dissociation, which leads to an intermediate state, and the subsequent T432$^{rot\text{-}A}$ O_γ–CII-ATP P_γ bond formation coupled with the proton transfer from T432$^{rot\text{-}A}$ O_γ to E318* O_ϵ. In the first part, 1D REUS was performed using q_1, whereas in the second part, we performed 2D REUS using two collective variables (Fig. 3A): q_1 and the proton transfer variable $q_2 = r_4 - r_3$, defined as the difference between two distances, r_3: E318* O_ϵ–T432$^{rot\text{-}A}$ H_γ and r_4: T432$^{rot\text{-}A}$ O_γ–T432$^{rot\text{-}A}$ H_γ. Harmonic restraints were applied along each coordinate with a force constant of 100.0 kcal mol^{-1} Å^{-2} in 1D-REUS and 50.0 kcal mol^{-1} Å^{-2} and 25.0 kcal mol^{-1} Å^{-2} along q_1 and q_2, respectively, in 2D-REUS. The restraints were centered at $q_1 = -1.0, -0.8, \ldots 2$ in 1D-REUS and $q_1 = 1.6, 1.8, \ldots 3.4$ and $q_2 = -1.5, -1.0, \ldots 2.0$ in 2D-REUS. The number of replicas in the 1D and 2D REUS simulations was thus 16 and 80, respectively. The rate of exchange attempts between replicas was fixed at 1 ps in all REUS calculations. The initial structures of the replicas were taken from the snapshots along the metaD trajectory. In the 2D REUS simulations, the initial structures were further generated by consecutively performing short (20 ps) 2D umbrella sampling simulations from the metaD snapshots along the positive and negative q_2 directions.

The replica was run for 820 and 620 ps in the 1D and 2D REUS simulations, respectively. The initial 120 ps was considered as the equilibration step and thus discarded from the following analyses. The 1D and 2D free energy surfaces (Fig. 3C and D) were constructed by the weighted histogram analysis method (67). The grid sizes along q_1 (1D surface), q_1 (2D surface), and q_2 (2D surface) were determined to be 0.05, 0.10, and 0.20 Å, respectively, after confirming that they do not affect the result. The free energies and SDs were calculated by the bootstrapping analysis (68). In particular, the trajectories with the same restraint were split into 50-ps-long pieces to construct individual histograms, and the bootstrapping of the histograms was performed within each restraint with equal probability. One hundred free energies surfaces were calculated from the bootstrapped histograms, and the free energy and error estimates were obtained as the mean and SD, respectively. The 1D free energy surface for the second part of the reaction was obtained as the minimum free energy path in the 2D free energy surface of q_1 and q_2. The two free energy surfaces were aligned at $q_1 = 1.6$ Å, and the free energy at the reactant ($q_1 = -1.0$ Å) was set to 0 kcal mol^{-1}. We note that aligning the two surfaces at points between 1.4 and 1.8 Å did not affect the result. The height of the free energy barrier was estimated from the 1D free energy surface, in which points between the grids were interpolated using the modified Akima interpolation algorithm (69) implemented in MATLAB.

To complement the QM/MM simulations and to explore the conformational states, e.g. the T432 rotamers in solution, MD simulation using classical mechanical force fields was performed from the equilibrated structure described above. The time step was set to 2 fs, and the MD simulation was performed under the constant-NVT (300 K) condition for 1 μs.

Acknowledgments

The calculations were partially done at the Research Center for Computational Sciences in Okazaki (23-IMS-C111 and 24-IMS-C105 to T.M. and 23-IMS-C196 to S.S.).

Supplementary Material

Supplementary material is available at *PNAS Nexus* online.

Funding

This study was supported by JSPS Grants-in-Aid for Scientific Research (22H04984, 24H02301, 22K19279, and 23H02448 to S.A.; 22K15051 to Y.F.; 22H02035, 23K23303, 23KK0254, 24K21756, and 25H02464 to T.M.; and 21H04676 and 23K17361 to S.S.) and partly by Takeda Science Foundation (to S.A.) and Toyoaki Scholarship Foundation (to S.A.).

Author Contributions

Y.F., T.M., and S.A. designed the research. Y.F. and Y.O. conducted biochemical experiments. Y.F. and S.A. analyzed structural data. T.M. and S.S. performed simulations. S.A., Y.F., and T.M. wrote the paper with input from all authors.

Preprints

This manuscript was posted on a preprint: https://www.biorxiv.org/content/10.1101/2024.03.21.584037v2.

Data Availability

All data relating to this study are presented in the manuscript and supplementary materials.

References

1 Pittendrigh CS. 1993. Temporal organization: reflections of a Darwinian clock-watcher. *Annu Rev Physiol*. 55:16–54.
2 Bell-Pedersen D, *et al.* 2005. Circadian rhythms from multiple oscillators: lessons from diverse organisms. *Nat Rev Genet*. 6: 544–556.
3 Takahashi JS, Hong H-K, Ko CH, McDearmon EL. 2008. The genetics of mammalian circadian order and disorder: implications for physiology and disease. *Nat Rev Genet*. 9:764–775.
4 Partch CL. 2020. Orchestration of circadian timing by macromolecular protein assemblies. *J Mol Biol*. 432:3426–3448.
5 Narasimamurthy R, Virshup DM. 2021. The phosphorylation switch that regulates ticking of the circadian clock. *Mol Cell*. 81: 1133–1146.
6 Tomita J, Nakajima M, Kondo T, Iwasaki H. 2005. No transcription-translation feedback in circadian rhythm of KaiC phosphorylation. *Science*. 307:251–254.
7 Anonymous. 2004. Chronobiology: biological timekeeping (book). *Choice: Cur Rev Acad Libraries*. 41:934.

8 Nakajima M, *et al.* 2005. Reconstitution of circadian oscillation of cyanobacterial KaiC phosphorylation in vitro. *Science*. 308: 414–415.
9 Chavan AG, *et al.* 2021. Reconstitution of an intact clock reveals mechanisms of circadian timekeeping. *Science*. 374:eabd4453.
10 Reinhardt R, Leonard TA. 2023. A critical evaluation of protein kinase regulation by activation loop autophosphorylation. *eLife*. 12:e88210.
11 Ishiura M, *et al.* 1998. Expression of a gene cluster kaiABC as a circadian feedback process in cyanobacteria. *Science*. 281: 1519–1523.
12 Pattanayek R, *et al.* 2004. Visualizing a circadian clock protein: crystal structure of KaiC and functional insights. *Mol Cell*. 15: 375–388.
13 Nishiwaki T, *et al.* 2004. Role of KaiC phosphorylation in the circadian clock system of *Synechococcus elongatus* PCC 7942. *Proc Natl Acad Sci U S A*. 101:13927–13932.
14 Nishiwaki T, *et al.* 2007. A sequential program of dual phosphorylation of KaiC as a basis for circadian rhythm in cyanobacteria. *EMBO J*. 26:4029–4037.
15 Rust MJ, Markson JS, Lane WS, Fisher DS, O'Shea EK. 2007. Ordered phosphorylation governs oscillation of a three-protein circadian clock. *Science*. 318:809–812.
16 Vakonakis I, *et al.* 2004. NMR structure of the KaiC-interacting C-terminal domain of KaiA, a circadian clock protein: implications for KaiA-KaiC interaction. *Proc Natl Acad Sci U S A*. 101: 1479–1484.
17 Pattanayek R, *et al.* 2006. Analysis of KaiA-KaiC protein interactions in the cyano-bacterial circadian clock using hybrid structural methods. *EMBO J*. 25:2017–2028.
18 Mori T, *et al.* 2018. Revealing circadian mechanisms of integration and resilience by visualizing clock proteins working in real time. *Nat Commun*. 9:3245.
19 Murayama Y, *et al.* 2011. Tracking and visualizing the circadian ticking of the cyanobacterial clock protein KaiC in solution. *EMBO J*. 30:68–78.
20 Mukaiyama A, *et al.* 2018. Conformational rearrangements of the C1 ring in KaiC measure the timing of assembly with KaiB. *Sci Rep*. 8:8803.
21 Mukaiyama A, Furuike Y, Yamashita E, Akiyama S. 2022. Highly sensitive tryptophan fluorescence probe for detecting rhythmic conformational changes of KaiC in the cyanobacterial circadian clock system. *Biochem J*. 479:1505–1515.
22 Furuike Y, *et al.* 2022. Elucidation of master allostery essential for circadian clock oscillation in cyanobacteria. *Sci Adv*. 8:eabm8990.
23 Mori T, Saito S. 2019. Conformational excitation and nonequilibrium transition facilitate enzymatic reactions: application to Pin1 peptidyl-prolyl isomerase. *J Phys Chem Lett*. 10:474–480.
24 Pattanayek R, *et al.* 2009. Structures of KaiC circadian clock mutant proteins: a new phosphorylation site at T426 and mechanisms of kinase, ATPase and phosphatase. *PLoS One*. 4:e7529.
25 Furuike Y, *et al.* 2022. Regulation mechanisms of the dual ATPase in KaiC. *Proc Natl Acad Sci U S A*. 119:e2119627119.
26 Chang Y-G, Kuo N-W, Tseng R, LiWang A. 2011. Flexibility of the C-terminal, or CII, ring of KaiC governs the rhythm of the circadian clock of cyanobacteria. *Proc Natl Acad Sci U S A*. 108: 14431–14436.
27 Swan JA, *et al.* 2022. Coupling of distant ATPase domains in the circadian clock protein KaiC. *Nat Struct Mol Biol*. 29:759–766.
28 Furuike Y, Yamashita E, Akiyama S. 2024. Structure-function relationship of KaiC around dawn. *Biophys Physicobiol*. 21:e210001.
29 Lassila JK, Zalatan JG, Herschlag D. 2011. Biological phosphoryl-transfer reactions: understanding mechanism and catalysis. *Annu Rev Biochem*. 80:669–702.
30 Roston D, Lu X, Fang D, Demapan D, Cui Q. 2018. Analysis of phosphoryl-transfer enzymes with QM/MM free energy simulations. *Methods Enzymol*. 607:53–90.
31 Cheng YH, Zhang YK, McCammon JA. 2005. How does the cAMP-dependent protein kinase catalyze the phosphorylation reaction: an ab initio QM/MM study. *J Am Chem Soc*. 127: 1553–1562.
32 Valiev M, Yang J, Adams JA, Taylor SS, Weare JH. 2007. Phosphorylation reaction in cAPK protein kinase-free energy quantum mechanical/molecular mechanics simulations. *J Phys Chem B*. 111:13455–13464.
33 Perez-Gallegos A, Garcia-Viloca M, Gonzalez-Lafont A, Lluch JM. 2014. A QM/MM study of the associative mechanism for the phosphorylation reaction catalyzed by protein kinase A and its D166A mutant. *J Comput Aided Mol Des*. 28:1077–1091.
34 Pérez-Gallegos A, Garcia-Viloca M, González-Lafont À, Lluch JM. 2015. SP20 phosphorylation reaction catalyzed by protein kinase A: QM/MM calculations based on recently determined crystallographic structures. *ACS Catal*. 5:4897–4912.
35 Perez-Gallegos A, Garcia-Viloca M, Gonzalez-Lafont A, Lluch JM. 2015. A QM/MM study of Kemptide phosphorylation catalyzed by protein kinase A. The role of Asp166 as a general acid/base catalyst. *Phys Chem Chem Phys*. 17:3497–3511.
36 De Vivo M, Cavalli A, Carloni P, Recanatini M. 2007. Computational study of the phosphoryl transfer catalyzed by a cyclin-dependent kinase. *Chemistry*. 13:8437–8444.
37 Recabarren R, Osorio EH, Caballero J, Tunon I, Alzate-Morales JH. 2019. Mechanistic insights into the phosphoryl transfer reaction in cyclin-dependent kinase 2: a QM/MM study. *PLoS One*. 14: e0215793.
38 Smith GK, Ke Z, Guo H, Hengge AC. 2011. Insights into the phosphoryl transfer mechanism of cyclin-dependent protein kinases from ab initio QM/MM free-energy studies. *J Phys Chem B*. 115: 13713–13722.
39 McClory J, Hu G-X, Zou J-W, Timson DJ, Huang M. 2019. Phosphorylation mechanism of N-acetyl-l-glutamate kinase, a QM/MM study. *J Phys Chem B*. 123:2844–2852.
40 Sanchez-Martinez M, Marcos E, Tauler R, Field M, Crehuet R. 2013. Conformational compression and barrier height heterogeneity in the N-acetylglutamate kinase. *J Phys Chem B*. 117: 14261–14272.
41 Chang Y-G, Tseng R, Kuo N-W, LiWang A. 2012. Rhythmic ring-ring stacking drives the circadian oscillator clockwise. *Proc Natl Acad Sci U S A*. 109:16847–16851.
42 Hubbard SR, Wei L, Ellis L, Hendrickson WA. 1994. Crystal structure of the tyrosine kinase domain of the human insulin receptor. *Nature*. 372:746–754.
43 Sicheri F, Moarefi I, Kuriyan J. 1997. Crystal structure of the Src family tyrosine kinase Hck. *Nature*. 385:602–609.
44 Xu W, Harrison SC, Eck MJ. 1997. Three-dimensional structure of the tyrosine kinase c-Src. *Nature*. 385:595–602.
45 von Raussendorf F, de Ruiter A, Leonard TA. 2017. A switch in nucleotide affinity governs activation of the Src and Tec family kinases. *Sci Rep*. 7:17405.
46 Wang Q, *et al.* 2015. Autoinhibition of Bruton's tyrosine kinase (Btk) and activation by soluble inositol hexakisphosphate. *eLife*. 4:e06074.
47 Goldberg J, Nairn AC, Kuriyan J. 1996. Structural basis for the autoinhibition of calcium/calmodulin-dependent protein kinase I. *Cell*. 84:875–887.

48 Rellos P, *et al.* 2010. Structure of the CaMKIIdelta/calmodulin complex reveals the molecular mechanism of CaMKII kinase activation. *PLoS Biol*. 8:e1000426.
49 Rosenberg OS, Deindl S, Sung R-J, Nairn AC, Kuriyan J. 2005. Structure of the autoinhibited kinase domain of CaMKII and SAXS analysis of the holoenzyme. *Cell*. 123:849–860.
50 Kim C, Cheng CY, Saldanha SA, Taylor SS. 2007. PKA-I holoenzyme structure reveals a mechanism for cAMP-dependent activation. *Cell*. 130:1032–1043.
51 Gebel J, *et al.* 2020. P63 uses a switch-like mechanism to set the threshold for induction of apoptosis. *Nat Chem Biol*. 16:1078–1086.
52 Isojima Y, *et al.* 2009. CKIepsilon/delta-dependent phosphorylation is a temperature-insensitive, period-determining process in the mammalian circadian clock. *Proc Natl Acad Sci U S A*. 106: 15744–15749.
53 Adams JA, Mcglone ML, Gibson R, Taylor SS. 1995. Phosphorylation modulates catalytic function and regulation in the cAMP-dependent protein kinase. *Biochemistry*. 34:2447–2454.
54 Orr JW, Newton AC. 1994. Requirement for negative charge on activation loop of protein kinase C. *J Biol Chem*. 269:27715–27718.
55 Ablooglu AJ, Kohanski RA. 2001. Activation of the insulin receptor's kinase domain changes the rate-determining step of substrate phosphorylation. *Biochemistry*. 40:504–513.
56 Boerner RJ, *et al.* 1996. Correlation of the phosphorylation states of pp60c-src with tyrosine kinase activity: the intramolecular pY530-SH2 complex retains significant activity if Y419 is phosphorylated. *Biochemistry*. 35:9519–9525.
57 Furuike Y, Abe J, Mukaiyama A, Akiyama S. 2016. Accelerating in vitro studies on circadian clock systems using an automated sampling device. *Biophys Physicobiol.* 13:235–241.
58 Lindorff-Larsen K, *et al.* 2010. Improved side-chain torsion potentials for the Amber ff99SB protein force field. *Proteins*. 78: 1950–1958.
59 Meagher KL, Redman LT, Carlson HA. 2003. Development of polyphosphate parameters for use with the AMBER force field. *J Comput Chem*. 24:1016–1025.
60 Jorgensen WL, Chandrasekhar J, Madura JD, Impey RW, Klein ML. 1983. Comparison of simple potential functions for simulating liquid water. *J Chem Phys*. 79:926–935.
61 Darden T, York D, Pedersen L. 1993. Particle mesh Ewald—an N log (N) method for Ewald sums in large systems. *J Chem Phys*. 98:10089–10092.
62 Case DA, *et al. AMBER18*. University of California, San Francisco, 2018.
63 Bonomi M, *et al.* 2009. PLUMED: a portable plugin for free-energy calculations with molecular dynamics. *Comput Phys Commun*. 180:1961–1972.
64 Gaus M, Cui QA, Elstner M. 2011. DFTB3: extension of the self-consistent-charge density-functional tight-binding method (SCC-DFTB). *J Chem Theory Comput*. 7:931–948.
65 Laio A, Parrinello M. 2002. Escaping free-energy minima. *Proc Natl Acad Sci U S A*. 99:12562–12566.
66 Sugita Y, Kitao A, Okamoto Y. 2000. Multidimensional replica-exchange method for free-energy calculations. *J Chem Phys*. 113:6042–6051.
67 Kumar S, Rosenberg JM, Bouzida D, Swendsen RH, Kollman PA. 1992. The weighted histogram analysis method for free-energy calculations on biomolecules. 1. The method. *J Comput Chem*. 13:1011–1021.
68 Hub JS, de Groot BL, van der Spoel D. 2010. G_wham-A free weighted histogram analysis implementation including robust error and autocorrelation estimates. *J Chem Theory Comput*. 6: 3713–3720.
69 Akima H. 1970. A new method of interpolation and smooth curve fitting based on local procedures. *J Assoc Comput Mach*. 17: 589–602.